Heliyon 10 (2024) e36000

Contents lists available at ScienceDirect

Heliyon

journal homepage: www.cell.com/heliyon

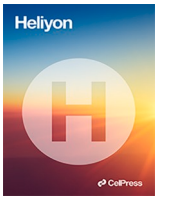

Research article

# Production and characterization of low-density silicon nitride reinforced zinc nanocomposite coatings on mild steel for applications in marine and automotive industries

I.G. Akande [a], R.A. Kazeem [b,c,*], O.O. Oluwole [b], T.C. Jen [c], E.T. Akinlabi [d]

[a] Department of Automotive Engineering, University of Ibadan, Ibadan, Nigeria
[b] Department of Mechanical Engineering, University of Ibadan, Ibadan, Nigeria
[c] Department of Mechanical Engineering Science, University of Johannesburg, Auckland Park, Johannesburg, 2006, South Africa
[d] Department of Mechanical and Construction Engineering, Faculty of Engineering and Environment, Northumbria University, Newcastle, NE1 8ST, United Kingdom

ARTICLE INFO

*Keywords:*
Corrosion rate
Zn-$Si_3N_4$
low density
Coatings
Mild steel
Wear volume

ABSTRACT

In today's automotive, marine and petrochemical industries, the desire for lightweight materials has increased. Hence, necessitating the production of components with low density. In this work, lightweight Zn–$Si_3N_4$ coatings were developed by including $Si_3N_4$ in the zinc matrix. The optimal coatings were produced on steel samples at 45 °C and varied $Si_3N_4$ particles and voltages following ASTM A53/A53M standard. The deterioration (corrosion) property i.e. corrosion rate (CR) and current density ($j_{ocorr}$) of the uncoated (control) and coated samples were examined in 0.5 M of sulphuric acid using a potentiodynamic polarization technique following ASTM G3/G102 standard. The microstructure of the samples was studied via the SEM micrographs and XRD patterns, while the wear performance resistance (following ASTM G99 standard) and electrical conductivity of the samples were examined with a pin-on-disc tribometer and ammeter-voltmeter. The corrosion experiment indicated that the uncoated mild steel specimen possessed a CR of 12.345 mm $year^{-1}$ and $j_{ocorr}$ of 1060 μA/$cm^2$, while the CR and $j_{corr}$ of the coated samples ranged from 2.6793 to 4.7975 mm $year^{-1}$ and 231−413 μA/$cm^2$, respectively. The lower CR and $j_{corr}$ values of the coated specimens, relative to the coated sample showed that the coatings possessed superior passivation ability in the test medium. The SEM micrographs of the samples showed refined morphology, while the XRD patterns revealed high peak intensity crystals such as $Zn_4SiN$, ZnNSi, $Zn_4N$ and $Zn_2NSi$, which could be beneficial to the mechanical properties and corrosion resistance of the steel. Moreover, the wear resistance study indicated that the COF of the uncoated sample ranged from 0.1 to 0.5, while those for coated specimens ranged from 0.05 to 0.35. Similarly, the uncoated steel exhibited a wear volume (WV) of 0.00508 $mm^3$, while the WV of the coated specimens ranged from 0.00266 to 0.0028 mm3, indicating the existence of high strengthening mechanisms between the interface of the protecting device and the steel. Also, the electrical conductivity of the mild steel sample reduced from 12.97 $\Omega^{-1}cm^{-1}$ to 0.64 $\Omega^{-1}cm^{-1}$, indicating that the electrical resistivity of the steel was enhanced by the coatings.

* Corresponding author. Department of Mechanical Engineering, University of Ibadan, Ibadan, Nigeria.
*E-mail address:* kazeemadebayo85@yahoo.com (R.A. Kazeem).

https://doi.org/10.1016/j.heliyon.2024.e36000
Received 10 June 2024; Received in revised form 15 July 2024; Accepted 7 August 2024
Available online 10 August 2024

## 1. Introduction

Silicon nitride ($Si_3N_4$) ceramic has a unique combination of material characteristics such as high strength and fracture toughness, intrinsic phase stability, high wear resistance, biocompatibility and hydrophilic in nature [1]. Rao and Mohan [2] studied the mechanical performance of $Si_3N_4$ reinforced aluminium metal matrix composite. The characterizations of the composite indicated that the 6 wt% optimal reinforcement enhanced the tensile strength and hardness of the matrix by 39 and 25 % respectively. Silicon nitride ceramic is also a well-known valuable and extensively used insulator, as in Matsunaga et al. [3], where the authors evaluated the dielectric breakdown of $Si_3N_4$ nitride substrates with various thickness using alternative current voltage. Due to reasonably high strength at ambient and elevated temperatures, excellent thermal shock and oxidation resistance, high-decomposition temperature, as well as a low coefficient of friction, silicon nitride has become one of the most widely used ceramic materials for advanced industrial applications in numerous environments such as the $Si_3N_4$ modified enamel coatings produced by Qian et al. [4], enable high thermal shock and corrosion resistances for steel protection. Ling et al. [5], Dergez et al. [6] and Khomenkova et al. [7] have also attested to the high chemical stability, good optical and electrical properties of silicon nitride ($Si_3N_4$). The good optical and electrical characteristics of silicon nitride were ascribed to its crystallographic structures and the broadband gap (5.3 eV) existing in the material. The $Si_3N_4$ unit cell comprises a $SiN_4$ tetrahedron where the nitrogen atoms surround the Si at the core. Hence, a solid structure is formed due to the three basic tetrahedral structural units which share nitrogen (N), as in recent publications by Ref. [8]. (2016) and Zhao et al. [9]. Due to this special structure exhibited by $Si_3N_4$, Logesh et al. [10] and Zhang et al. [11] explored the reinforcement ability of $Si_3N_4$ ceramic by incorporating it in matrix composites. In like manner, many researchers have reinforced alloys using $Si_3N_4$ ceramic.

For instance, ductile LM25 Al alloy was reinforced with hard $Si_3N_4$ by Ahmad et al. [12]. Amongst the numerous reasons for the authors' preference for silicon nitride were its unique characteristics such as low density, good fatigue strength and high corrosion resistance. The inclusion of $Si_3N_4$ to the fragile LM 25 led to the enhancement in strength as a result of the tensile strength transferred to the tightly bonded silicon nitride which improved the density of dislocation and consequently resulted in the strengthening of the grains. The hard $Si_3N_4$ was also adjudged by Reddy et al. [13] to have increased the resistance to deformation by forming barriers or clouds in the path of defects motion. Similarly, Arya and Telang [14] used silicon nitride ($Si_3N_4$) as reinforcement for AA6082 alloy. The excellent microstructural properties and strength of the developed composite were attributed to the excellent wettability, intermetallic strength and even dispersal of the silicon nitride within the alloy's matrix. Moreover, Zgalat-Lozynskyy et al. [15] investigated the mechanical strength of $Si_3N_4$ particles by including them in polypropylene (PP) and polyethylene (PE) for 3D printing. The wear performance assessment of the PE–$Si_3N_4$ and PP–$Si_3N_4$ composites showed that a rise in the concentration of silicon nitride particles resulted in the improved wear resistance of the composites. The minimal abrasive wear of the $Si_3N_4$ particles-reinforced polypropylene and polyethylene materials while in contact with the indenting material revealed that the composite possessed reasonably high fracture resistance in 3D printing.

The mechanical behaviour of silicon nitride ($Si_3N_4$) particles reinforced copper-tin matrix composites was in the same vein investigated by Hanumantharayappa et al. [16]. The strength hardness and ultimate tensile of the copper-tin matrix by improved 41 % and 33 %, respectively, due to the incorporation of $Si_3N_4$ particles. Therefore, the abovementioned outstanding characteristics of $Si_3N_4$ particles have impelled its addition to zinc (Zn) for the improvement in the properties of carbon steel in this work. Zinc (Zn) rich coating has been reported by Cheng et al. [17] to exhibit micro-pores which act as crevices for the initiation of corrosion and other environmental attacks. Thus, in this work, $Si_3N_4$ was incorporated in a zinc matrix to develop Zn–$Si_3N_4$ coatings whose corrosion, microstructural and wear resistance properties were further investigated.

## 2. Materials and methods

### 2.1. Preparation of substrates and coating bath formulation

The percentage of elements in the steel plate used as the cathode are indicated in Table 1. The flat steel plate was sectioned into specimens of length 45 mm, width 25 mm and thickness 2 mm. Similarly, the zinc anodes contain 99.9 % zinc and, are of 55 mm × 35 mm × 10 mm. The polishing and de-scaling of the steel specimens were carried out using 90, 120 and 180 grit-sized emery papers. At the temperature of 25 °C, the polished samples were then cleaned and degreased for 10 s using 0.01 M sodium carbonate. The degreased steel specimens were further pickled in 10 % HCl for 10 seconds to remove impurities. The samples were afterwards rinsed in distilled water before starting the coating. Table 2 shows the coating bath. This bath could be referred to as a sulphate bath due to the predominance of the sulphate reagents such as potassium sulphate, sodium sulphate and zinc sulphate. The optimum mass concentrations of silicon nitride were determined after several preliminary investigational runs.

**Table 1**
Percentage of elements in the steel.

| Constituent | Si | C | P | Mn | S | Cr | Ni | Cu | Fe |
|---|---|---|---|---|---|---|---|---|---|
| Percentage | 0.155 | 0.210 | 0.024 | 0.469 | 0.025 | 0.023 | 0.007 | 0.005 | Bal. |

### 2.2. Electrodeposition procedure

The coatings were achieved following the ASTM A53/A53M criterion for steel coating. In the electrodeposition set-up, the cathode (mild steel) and the zinc anodes were respectively linked to the negative and positive terminal of a rectifier as indicated in Fig. 1. The zinc anodes were positioned some distance apart in the bath, and the cathode was located 3 cm from the respective anodes, for easy circulation of ions. The rectifier was plugged into the main power source for the deposition process to begin. The depositions were completed at the temperature, cell voltages, time, current density, stirring rate and pH of 45 °C, 0.3/0.5 V, 15 min, 1.5 A/cm$^2$, 250 rpm and 4.5, respectively. The aforementioned process parameters were kept constant except for the cell voltage. The stirring of the bath constituents was maintained to ensure uniform dispersion of particles on the steel. The continuous stirring of the bath also enhances electrophoresis mobility. At the end of the 15 min of each coating, the coated samples were disconnected from the terminals and rinsed slightly in distilled water to remove any salt deposits and crumbs of particles from the coated mild steel surface. The reactions that took place between the zinc and the iron are indicated in Eqns. (1)–(3), which are the reduction reaction, oxidation reaction and the combined cell reaction, respectively.

$$Fe^{2+} + 2e^{-} \rightarrow Fe \text{ (at the cathode)} \quad (1)$$

$$Zn \rightarrow Zn^{2+} + 2e^{-} \text{ (at the anode)} \quad (2)$$

$$Fe^{2+} + Zn \rightarrow Fe + Zn^{2+} \quad (3)$$

### 2.3. Samples characterization

Before the characterization, samples were cut to 10 mm × 10 mm × 2 mm. The thickness of the film was studied using a thickness-measuring device with accurateness of ±0.0001 mm. The thickness of the coating on each sample was measured at three points and the average was documented. The samples' surface microstructure was studied employing SEM equipped with EDS. The SEM images were 500 times the magnification of the samples. The crystallographic structure of the samples was examined using the X-ray diffractometer (XRD). With the XRD patterns, the intensity of the phases in the crystalline materials was revealed. The corrosion resistance ability of the specimens was investigated in 0.5 M of sulphuric acid in accord with ASTM G102 criterion for corrosion test at 25 °C, using the PGSTAT 101 auto lab. The samples were soldered to copper wires and embedded epoxy resins, leaving exposed 10 × 10 mm$^2$ of the samples' surface area to the acidic medium. The corrosion investigation setup comprises a graphite rod (counter electrode); calomel electrode (reference electrode) and working electrode (coated and uncoated steel samples). The electrodes were inserted in the 0.5 M $H_2SO_4$ solution, and the test was run for 60 min at −1.5 V (start potential) and 1.5 V (stop potential) vs. OCP at a scan rate of 0.005 V/s using NOVA 2.1.2 software. From the Tafel extrapolation, the $E_{corr}$ and $j_{corr}$ were estimated. The PR, CR and CE were evaluated with Eqns. (4)–(6), respectively.

Polarization resistance

$$PR = 2.303 b_a b_c / j_{corr}(b_a + b_c) \quad (4)$$

Corrosion rate,

$$CR = \left(0.00327 \times j_{corr} \times w_{eq}\right) / \rho \quad (5)$$

Coating efficiency,

$$CE = [1 - (j_{corr} / j_{ocorr})] \times 100 \quad (6)$$

where weq (g) is the specific weight of samples, ρ (g/cm$^3$) is the samples density, $j_{ocorr}$ and $j_{corr}$ (A/cm$^2$) are the current density of the samples, bc is the cathodic slope, ba is the anodic slope, while 2.303 and 0.00327 are the constants. The samples' wear characteristics were evaluated in accord with ASTM G99 criterion employing a tribometer (pin-on-disk) at 50 % RH, 25 °C, 10 Hz sliding frequency, 2.5 mm/s sliding velocity with a ball of Ø 2.5 mm, which was subjected to 20 N of load. The distance of slide was 5 mm for 3 min. Also, in accord with ASTM A587 standard of electrical resistance measurement, the electrical conductivity of the specimens was examined. This was achieved using ammeter-voltmeter to read the current and voltage across the samples. The resistance across the

**Table 2**
Coating bath composition.

| Composition | Concentration (g/L) |
|---|---|
| $K_2SO_4$ | 50 |
| $Na_2SO_4$ | 30 |
| $ZnSO_4$ | 130 |
| NaCl | 35 |
| Glycine | 10 |
| Boric acid | 10 |
| Thiourea | 10 |
| Silicon nitride | 7/13 |

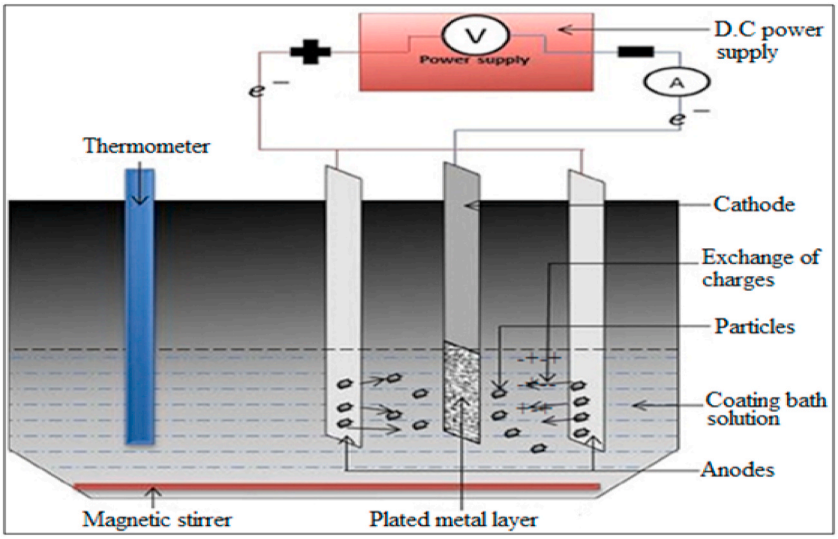


**Fig. 1.** Schematic of Electrodeposition process [18].

specimens was thereafter evaluated. Consequently, the electrical conductivity of the samples was calculated using Eqn. (7).

$$C = L/RA \tag{7}$$

where L, R and A are the length of the samples, resistance and surface area of the specimens, respectively.

## 3. Results and discussion

### 3.1. Thickness of Zn–$Si_3N_4$ coatings and weight gained by samples

Fig. 2a and b indicated the coating thickness and weight gained by samples, respectively. The 0.3Zn–7$Si_3N_4$ coating possessed the least thickness of 138.20 μm, whereas the coating at 0.5 V with 13 g of $Si_3N_4$ possessed 175.70 μm, which is the utmost coating thickness. The increase in cell voltage and concentration of silicon nitride could have been the reason for the soar in coating thickness. Nevertheless, the 0.3Zn–13$Si_3N_4$ coated steel possessed an unexpected trend despite the high concentration of $Si_3N_4$ nanoparticles. Other process parameters could have influenced the thickness of 0.3Zn–13$Si_3N_4$ coating. However, increasing the mass of nanoparticles in the deposition bath could have increased the thickness of the coating and decreased the coating surface coarseness. Nonetheless, process parameters could have several influences on the texture of coatings by changing the performance of coatings as reported by Zheng et al. [19]. The properties of thin films are often enhanced by the dispersed particles' stability. High coating thickness could at times not correspond to superior coating stability. Hence, coating thickness of acceptable standard with outstanding

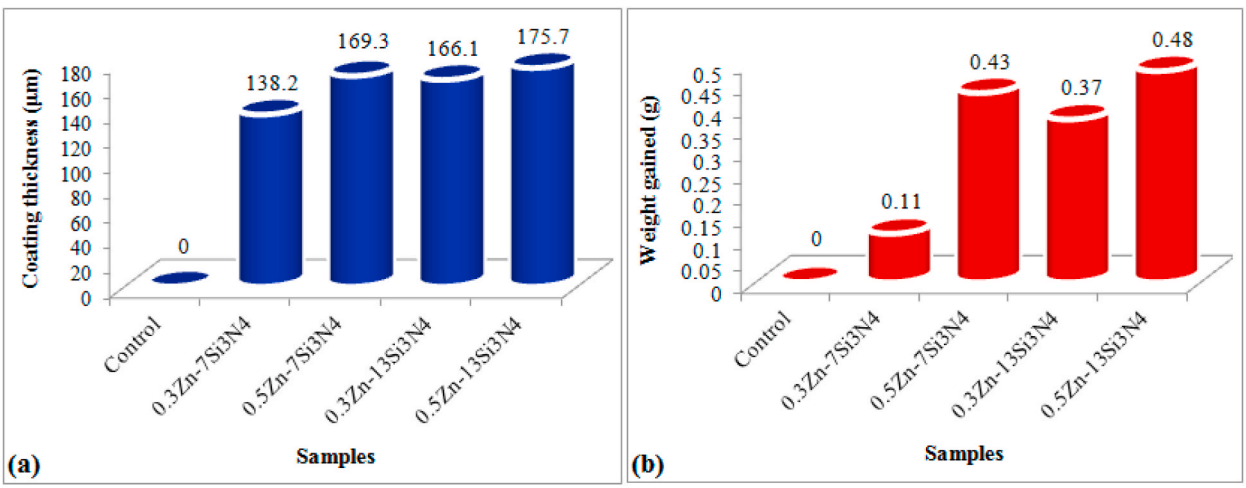


**Fig. 2.** (a) Coating thickness and **(b)** Weight gained by samples.

texture and particle stability is essential. Fascinatingly, the entire coatings exhibited significant degrees of thickness and satisfactory weight (see Fig. 2 b) due to the optimized deposition time, applied cell voltage and dispersal ability of the nanoparticles, which are crucial to the improvement of surfaces such as mild steel.

### 3.2. Corrosion characteristics of Zn–$Si_3N_4$ coatings

Figs. 3–7 indicated the corrosion performance of the samples in 0.5 M of $H_2SO_4$. The Zn–$Si_3N_4$ coated samples possessed a lower corrosion rate (CR) relative to the uncoated steel (control). The 0.5Zn–13$Si_3N_4$ coated steel possessed the lowest CR of 2.6793 mm $year^{-1}$, while the control possessed the uppermost CR of 12.345 mm $year^{-1}$. Due to the utmost polarization resistance (PR), lowest corrosion rate and least current density possessed by the 0.5Zn–13$Si_3N_4$ coated steel as indicated in Figs. 3–5, the 0.5Zn-13 $Si_3N_4$ coating was adjudged to possess the best corrosion resistance, relative to the other coatings. In general, the Zn–$Si_3N_4$ coatings exhibited a noteworthy decrease in corrosion rate, which showed that the coatings inhibited the steel's active sites from the infiltration of corrosive ions, as affirmed by Akande et al. [20]. Thus, inhibition of the steel by the composite coatings could have been responsible for the outstanding resistance of the coated samples to deterioration in the $H_2SO_4$ medium. The Tafel plots in Fig. 6 showed that the $E_{corr}$ of specimens are not far apart. The corrosion potential ($E_{corr}$) of samples ranged from −0.7337 to −0.5652 V. Hence, the coatings largely protected the cathodic site of the steel in this test medium due to the shift of the $E_{corr}$ to a more negative region, though it also affected the anodic site to some level, as similarly reported by Fayomi et al. [21]. Fig. 7 additionally indicates the efficiency of coatings in the corrosive solution. The efficiency of Zn–$Si_3N_4$ coatings was estimated to be above 60%. The 0.5Zn–13$Si_3N_4$ sample possessed the uppermost efficiency of 78.3 % in the acidic medium, which indicated possible applications in automotive, marine and petrochemical industries. Fig. 8 further indicated the OCP (open circuit potential) versus time graphs for the samples in the acidic solution. Comparing the $E_{ocp}$ of the samples to the $E_{corr}$, it was observed that the samples were positively polarized. Thus, positive or anodic polarization reduces corrosion rate extensively as indicated by Deyab et al. [22] and Qin et al. [23]. The specimens accomplished steady-state within the test period. The Zn–$Si_3N_4$ films were observed to have also shifted the OCP of the steel (control) to a more negative region, which implied the predominant cathodic inhibition effect of Zn–$Si_3N_4$ coatings in the acidic solution.

### 3.3. Microstructure of samples

#### 3.3.1. SEM and EDS images of samples

Fig. 9 indicated the SEM and EDS of the control sample (base material). The sample exhibited morphology irregularity and pitting evolution tendency. Some dark spots observed on the surface suggest that corrosion products could turn out to be noticeable to the bare eye soon if the steel is not protected. The EDS showed that iron (Fe) is predominant in steel. Elements such as silicon, manganese and carbon, were also present in little quantities. The SEM and EDS of $Si_3N_4$ particles are shown in Fig. 10. The particles were observed to possess even-sized grains. The SEM image exhibited grey nodule-like particles free from impurities, which showed that the deposition bath was unadulterated. Fig. 9 also indicated that the EDS exhibited silicon and nitrogen which are the main elements in $Si_3N_4$. The SEM images and EDS of the nanocomposite coatings are shown in Figs. 11–14. The coatings exhibited outstanding morphology and exceptional particle distribution. The 0.5Zn–7$Si_3N_4$ coating exhibited coarse grains and a lot of grey flake-like structure, while the 0.3Zn–7$Si_3N_4$ coating possessed finer grains with a sparkling appearance. More presence of nanocrystalline layers of the particle was observed on the 0.3Zn–7$Si_3N_4$ coatings, which could enhance the anti-dissolution ability of the coating as affirmed by Li et al. [24]. Fig. 12 indicated that the 0.5Zn–7$Si_3N_4$ coating was more permeable, exhibiting several splits relative to the 0.3Zn–7$Si_3N_4$ coating. The disparity in the transportation rapidity of zinc to the steel cathode could have caused the variation in the coatings. In agreement with Praveenkumar et al. [25] assertion, the 0.5Zn–7$Si_3N_4$ coating perhaps contained in the matrix more Zn, whose growth needs retardation by more nanoparticles. More nanoparticles could have been present in 0.3Zn–7$Si_3N_4$ deposit thus minimizing the grain size of the coating. As indicated in Figs. 13 and 14, the coatings at 0.3 and 0.5 V, with 13 g of $Si_3N_4$ contained a larger mass of silicon nitride. The coatings exhibited good coverage, and it was evenly dispersal. The zinc boundary of the coatings exhibited a more nodule-like structure with refined morphologies. The increase in the mass of silicon nitride could have led to the embedment of an additional quantity of nanoparticles in the deposits. Nevertheless, surpassing the optimal quantity required may lead to the clustering of $Si_3N_4$ nanoparticles, and thus decreases further adsorption of silicon nitride into the matrix of the coating. Relatively, the 0.5Zn–13$Si_3N_4$

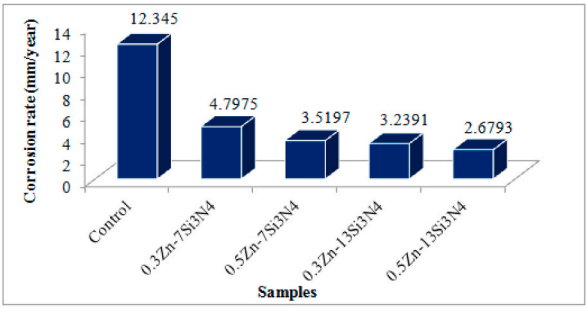


**Fig. 3.** Corrosion rate of samples.

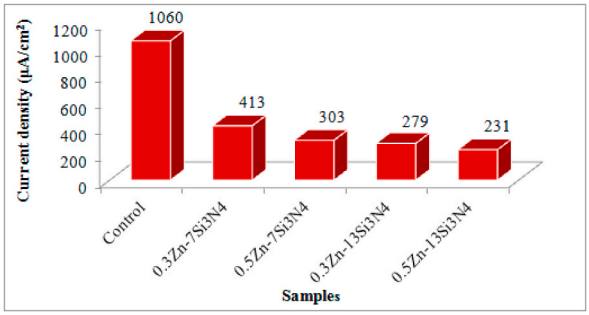


**Fig. 4.** Corrosion current density of samples.

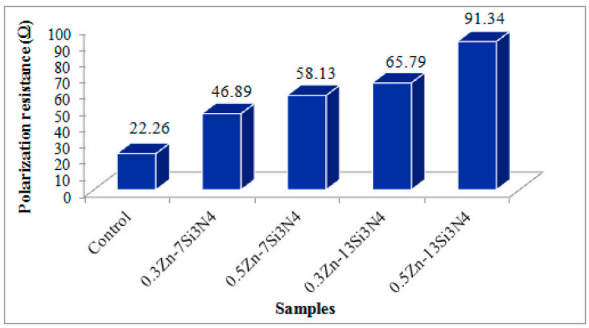


**Fig. 5.** Polarization resistance of samples.

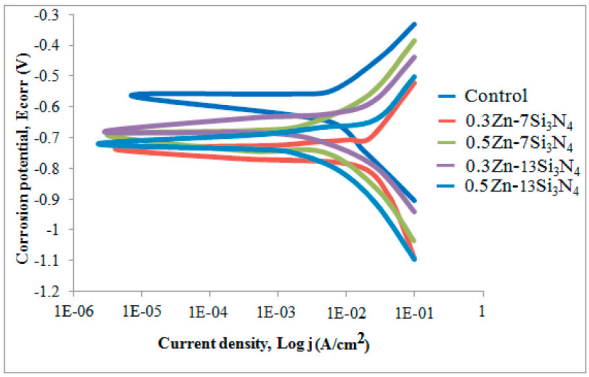


**Fig. 6.** Tafel plots for samples.

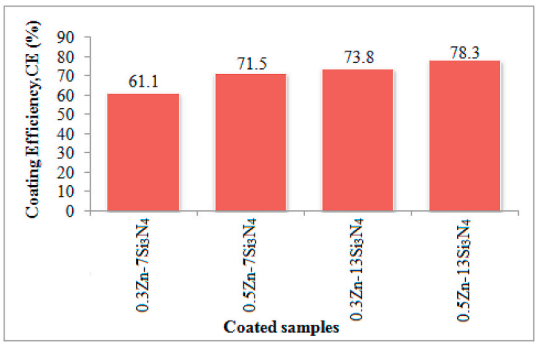


**Fig. 7.** Efficiencies of Zn–$Si_3N_4$ coatings.

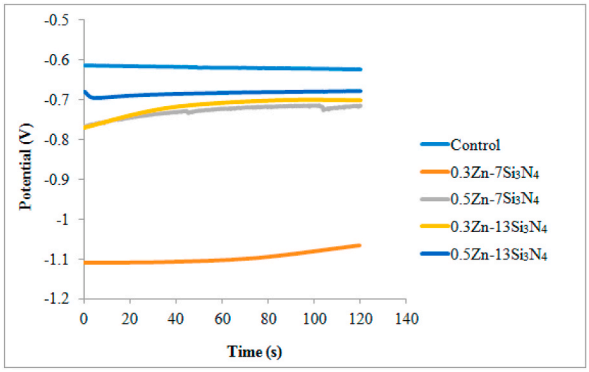


**Fig. 8.** Plot of OCP against time for samples.

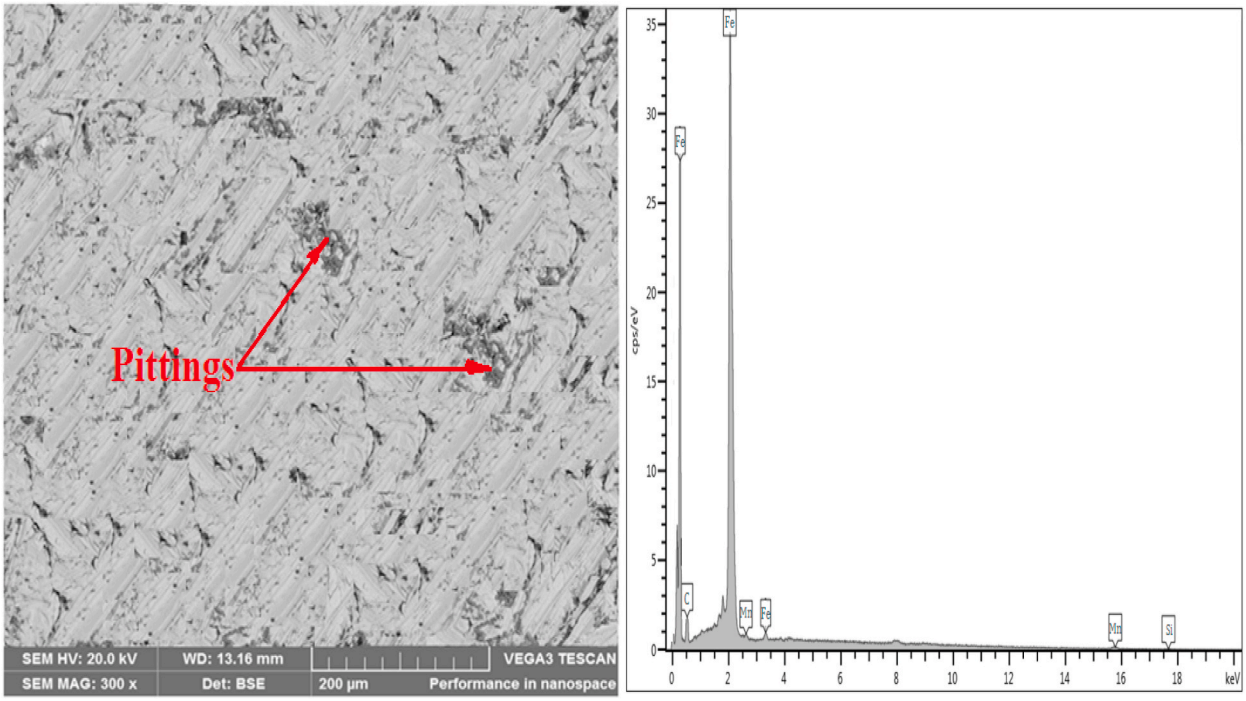


**Fig. 9.** SEM and EDS of the uncoated steel.

coating exhibited superior morphology and better microstructure compared to the other samples. The outstanding surface morphology and structure of 0.5Zn–13$Si_3N_4$ coating may perhaps be attributed to good dispersion of the particles, and the influence of process parameters such as deposition temperature, cell voltage, coating time, pH and the optimal mass of silicon nitride in the bath. The EDS examination of the coatings shown in Figs. 11–14 indicated the existence of Si, N and Zn. The EDS also indicated the predominant deposition of Zn which was anticipated since silicon nitride particles are strengthening ingredients incorporated in minute quantities to integrate specific properties lacking in zinc and steel.

### *3.4. XRD patterns of Zn–$Si_3N_4$ coated steel*

Figs. 15 and 16 respectively indicated the XRD patterns of coatings at 0.3 and 0.5 V, with 7 g of $Si_3N_4$. The film surfaces were observed to possess high peaks and distinct phases. The 0.3Zn–7$Si_3N_4$ coating matrix exhibited ZnON, $Zn_2Si$, $Zn_2N$ and $Zn_4SiN$ phases, while the 0.5Zn–7$Si_3N_4$ coating possessed crystallographic phases such as $Zn_2Si$, ZnNSi, ZnON and ZnN phases. The elements Si, N and Zn of the strengthening $Si_3N_4$ did not occur as a single peak, revealing that the $Si_3N_4$ particles combined evenly with zinc particles to produce crystallographic phases. The 0.3Zn–7$Si_3N_4$ sample exhibited a distinctive phase of $Zn_4SiN$ crystalline, observed at the highest intensity of 6322 a.u and 2theta of 42.35°. ZnON at 2theta of 81.36° and 53.48°, $Zn_2N$ at 2theta of 69.26° and $Zn_2Si$ at 2theta of 35.41° are the other crystallographic phases of high intensities detected in the 0.3Zn–7$Si_3N_4$ coating. Likewise, in the 0.5Zn–7$Si_3N_4$ sample,

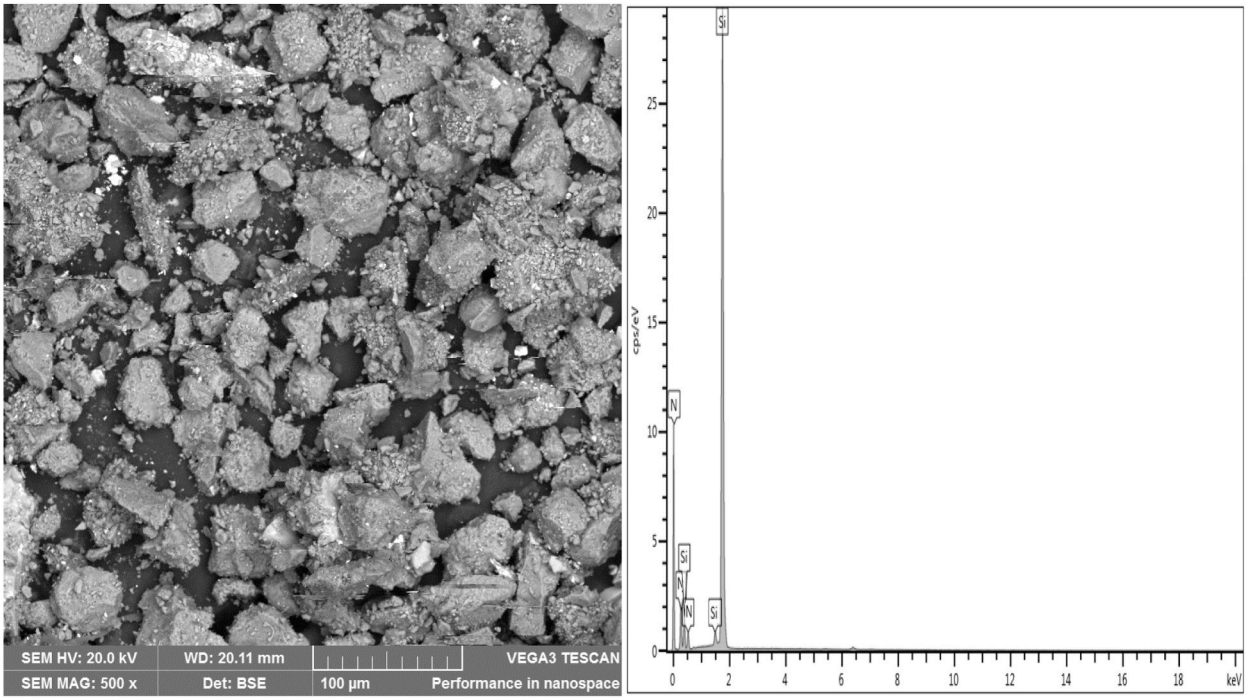


**Fig. 10.** SEM and EDS of $Si_3N_4$ particles.

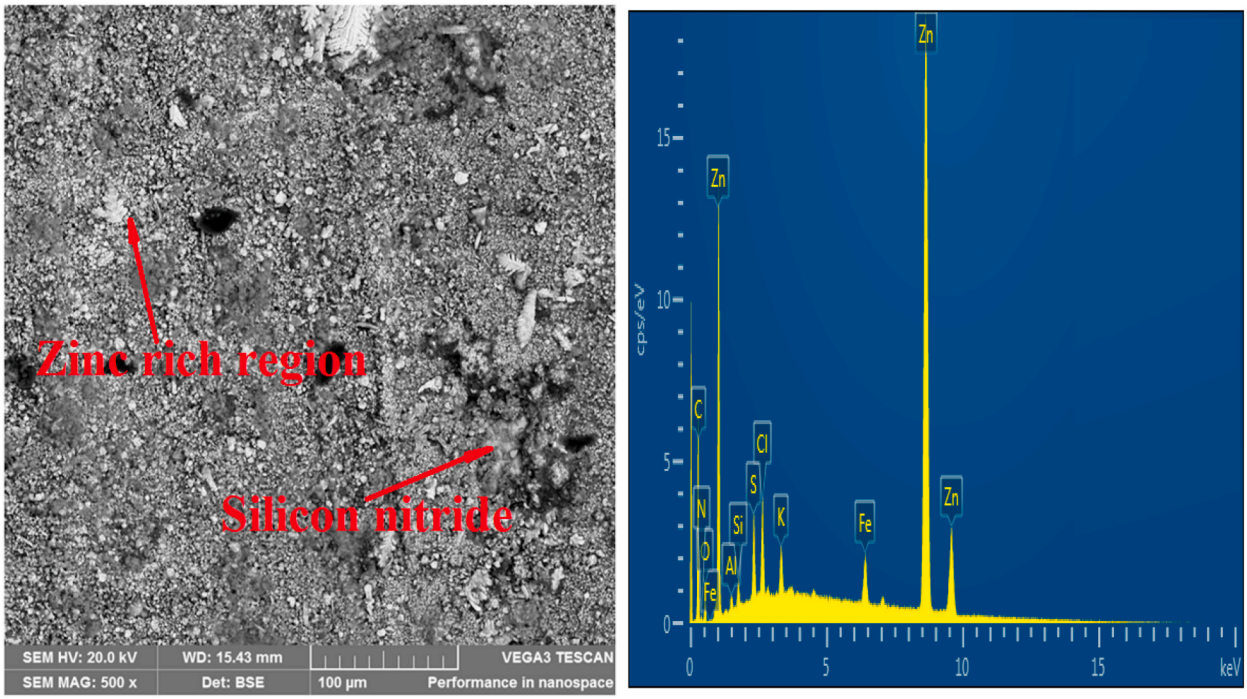


**Fig. 11.** SEM and EDS of 0.3Zn–7$Si_3N_4$ coating.

major peaks of ZnON at 2theta of 85.85°, ZnN at 2theta of 69.26° and 81.40°, $Zn_2Si_2$ at 2theta of 53.46° and $ZnN_2Si$ at 2theta of 42.36° were observed. The distinctiveness of these crystallographic phases is a sign that a complete dissolution of the particles was accomplished. Moreover, the peak heights indicated the outstanding quality of the phases. The phases also suggestively show that silicon nitride particles were effectively added to the developed coating, which is in agreement with the affirmation of Li et al. [24].

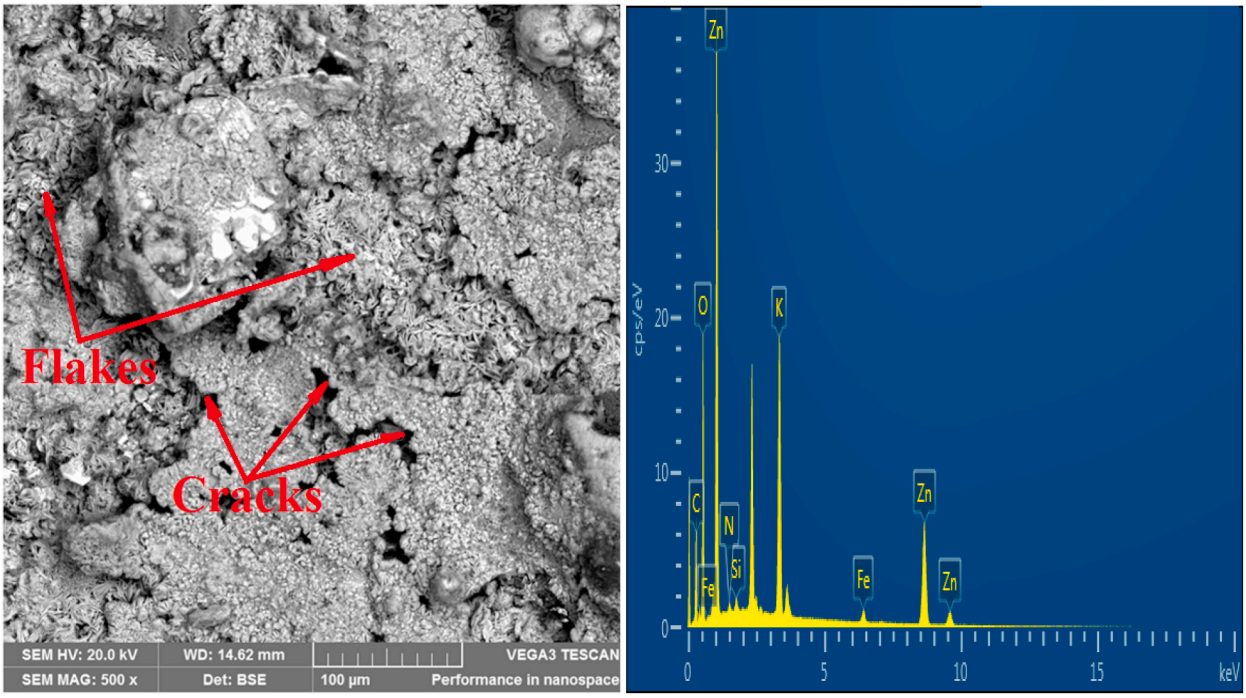


**Fig. 12.** SEM and EDS of 0.5Zn–7$Si_3N_4$ coating.

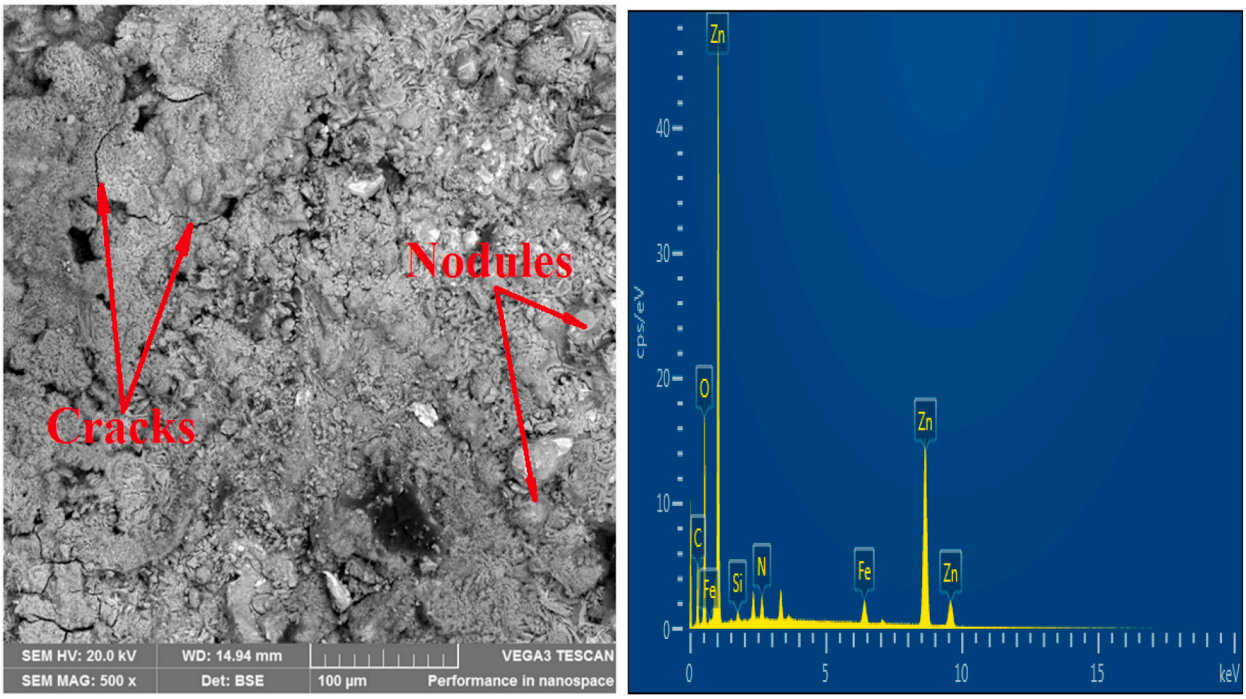


**Fig. 13.** SEM and EDS of 0.3Zn–13$Si_3N_4$ coating.

Furthermore, Figs. 17 and 18 indicated that the XRD patterns of the coatings with 13 g of $Si_3N_4$ coatings. These coatings were observed to exhibit superior intensities relative to those with the coating with 7 g of $S_{i3}N_4$, which indicated that the mass concentration of particles, played an important role in the intensities of the phases since the nanoparticles are evenly dispersed. The coating at 0.3 V, with 13 g of $Si_3N_4$ exhibited the utmost peak intensity of 7512 a.u at 2theta of 42.33$^o$ for ZnOSi crystallite. Also, the coating at 0.5 V,

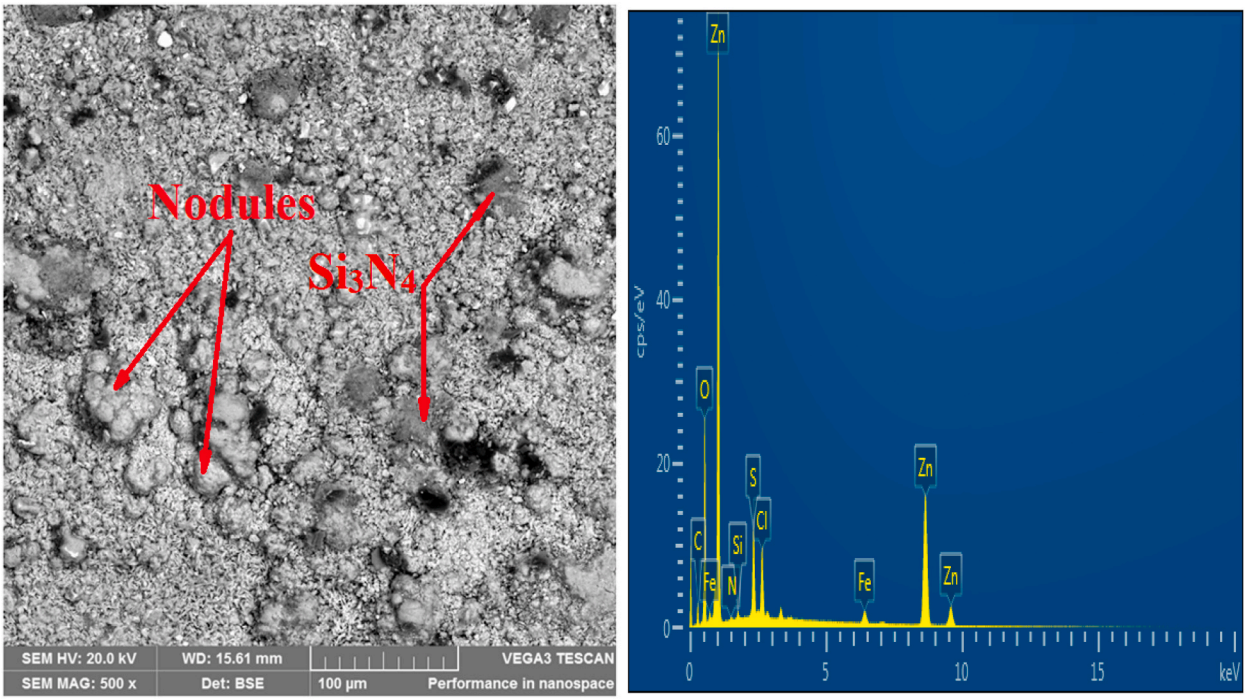


**Fig. 14.** SEM and EDS of 0.5Zn–13$Si_3N_4$ coating.

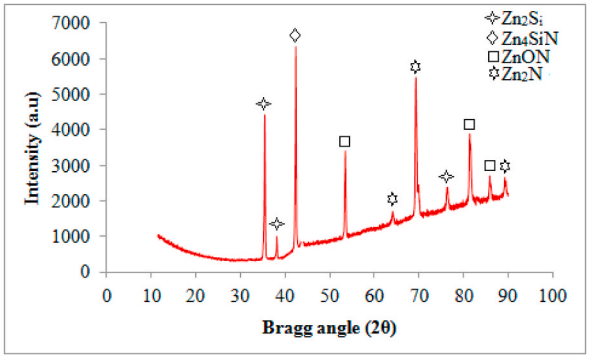


**Fig. 15.** XRD pattern for 0.3Zn–7$Si_3N_4$ coating.

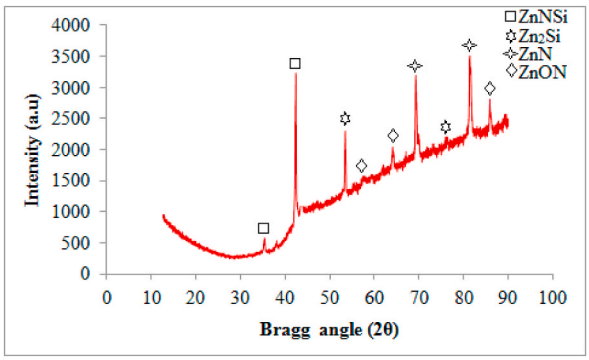


**Fig. 16.** XRD pattern for 0.5Zn–7$Si_3N_4$ coating.

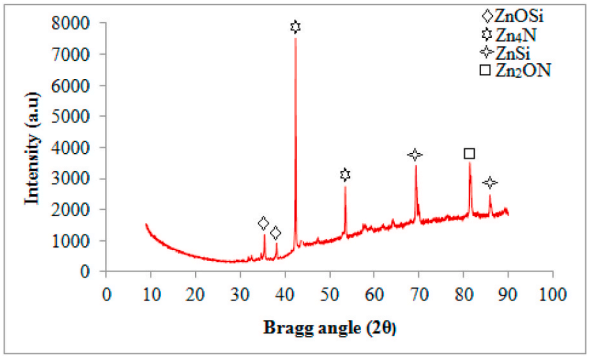


**Fig. 17.** XRD pattern for 0.3Zn–13$Si_3N_4$ coating.

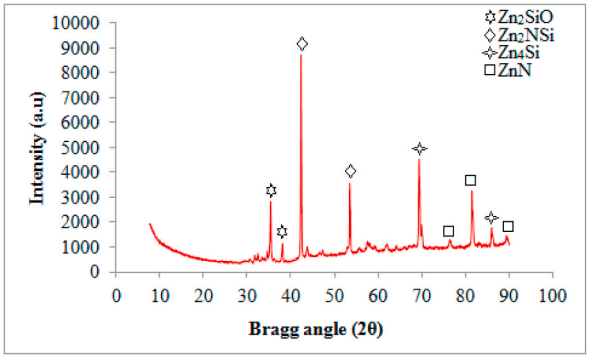


**Fig. 18.** XRD pattern for 0.5Zn–13$Si_3N_4$ coating.

with 13 g of $Si_3N_4$ possessed the uppermost peak intensity of 8750 a.u at 2theta of 42.38°. The silicon nitride particles were observed to have modified in the crystallographic orientation as affirmed by Sheng et al. [26].

### 3.5. *Wear characteristics of samples*

The wear volume (WV) of the samples is indicated in Fig. 19. The control possessed greater wear loss relative to the coated steel. The deposition potential and additives concentration of the thin films were observed to have influenced the WV. The wear volume of the control was 0.00508 mm3, which is higher than those of the coated samples. The decrease in the WV of the coated steel showed that the Zn–$Si_3N_4$ film functioned as a plastic deformation barrier. Comparing the entire samples, the 0.5Zn–13$Si_3N_4$ coating exhibited the

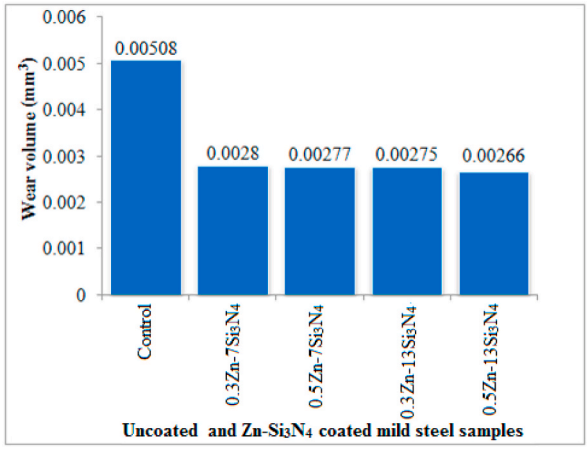


**Fig. 19.** Wear volume of the samples.

lowest and superior WV of 0.00266 $mm^3$. The low wear volume of the coated specimens could be ascribed to the capability of the coatings to prevent motion of dislocation on the steel surface. This scenario was similarly attested to by Enyi et al. [27].

The silicon nitride could have reduced particle detachment (PD) and micro-segregation (M−S). The decrease in PD and M−S could be the reason for the strong interface bond linking the mild steel surface and the Zn–$Si_3N_4$ coating layer, thus decreasing the WV of the coatings. To establish the pill-off decreasing effect of the coatings on the steel, the COF of the samples was examined as shown in Fig. 20, which in addition showed the wear characteristics of the specimens under the sliding load. The coated samples possessed substantially low COF relative to the control sample, which indicated that the coatings extensively minimized the force of friction existing in-between the sliding ball and the steel. The coatings also minimized the ball transverse rate on the steel. This is obvious in the significantly low COF. The COF-reducing effect of silicon nitride was also reported by Kumar and Venkatesha [28]. The authors attributed the wear resistance performance of silicon nitride to its lubricity and ability to absorb heat energy, which consequently reduces the friction of sliding materials. The SEM image of the wear scar of the control sample is shown in Fig. 21. The control sample was observed to exhibit irregular and deep grooves. Abrasive and adhesive wear losses could largely have taken place due to the wear debris volume that fell off the sample. Moreover, the SEM micrographs of the coated steel are indicated in Figs. 22–25. On the Zn–$Si_3N_4$ coatings wear scars morphology was observed to have a few grooves and low volume of wear debris (WD). The low volume of WD indicated that the coatings provided the mild steel with stability and significantly high resistance to deformation. Relative to the other coated samples, the SEM image of the coating at 0.5 V, with 13 g of $Si_3N_4$ exhibited superior morphology, the least quantity of wear debris and extremely low furrows or grooves. These are validations of the least COF and wear volume it exhibited.

### 3.6. Electrical conductivity (EC) of the samples

The EC of the samples is indicated in Fig. 26. The control sample possessed the utmost EC value of 12.970 $\Omega^{-1}cm^{-1}$. The Zn–$Si_3N_4$ coatings provided insulation for the steel sample, resulting in a remarkable reduction in the EC. The reduction in the EC also signified that the coatings improved the electrical resistivity (ER) of the mild steel. The enhancement in ER of the steel may be ascribed to the availability of silicon nitride in the coating. The ER enchantment ability of silicon nitride was acknowledged by Liang et al. [29]. The coating at 0.3 V with 13 g of $Si_3N_4$ possessed the least electrical conductivity, indicating that it possessed better insulating properties. This enhancement in electrical resistivity is substantial in electrical applications.

## 4. Conclusions

i) The thickness of the coatings ranged from 138.2 to 175.7 μm, which showed that a thin film was developed on the steel.
ii) The 0.5Zn–13$Si_3N_4$ coated steel, which exhibited superior resistance relative to the other specimens possessed a corrosion rate (CR) of 2.6793 mm $year^{-1}$, while the uncoated steel possessed a CR of 12.345 mm $year^{-1}$. This showed that the steel surface was made passive by the coating, hence reducing the penetration of the ions from the acidic solution.
iii) The SEM micrographs of the samples showed that the coated specimens possessed good morphology, while the XRD patterns revealed high peak intensity crystals such as $Zn_4SiN$, ZnNSi, $Zn_4N$ and $Zn_2NSi$.
iv) Moreover, the wear resistance study indicated that the uncoated sample exhibited a wear volume (WV) of 0.00508 $mm^3$, while the WV of the coated specimens ranged from 0.00266 to 0.0028 $mm^3$. Similarly, the COF of the uncoated sample ranged from 0.1 to 0.5, while the coated samples ranged from 0.05 to 0.35, indicating the existence of high strengthening mechanisms in between the interface of the steel and the coatings.
v) The electrical conductivity of the steel reduced from 12.97 $\Omega^{-1}cm^{-1}$ to 0.64 $\Omega^{-1}cm^{-1}$, indicating that the electrical resistivity was enhanced by the coatings.

## CRediT authorship contribution statement

**I.G. Akande:** Writing – original draft, Revision of manuscript, Methodology, Validation, Investigation, Data curation,

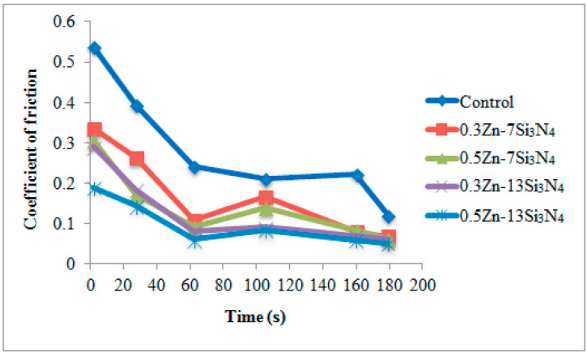


**Fig. 20.** COF of the samples.

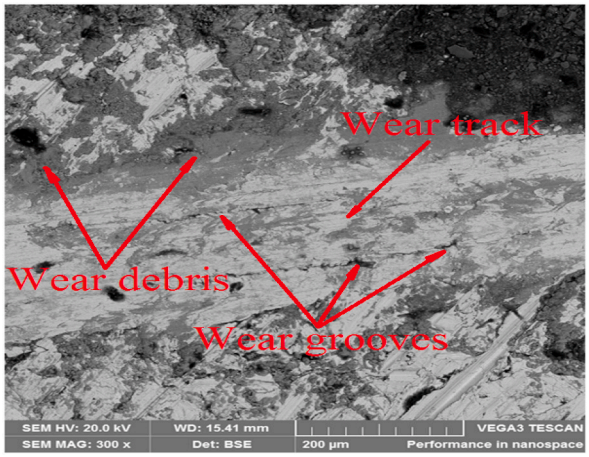


**Fig. 21.** SEM image of wear scar on the control sample.


**Fig. 22.** SEM image of the wear scar on 0.3Zn–7$Si_3N_4$sample.

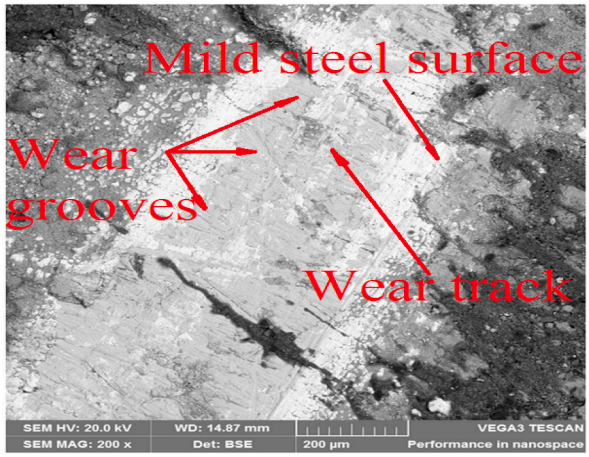


**Fig. 23.** SEM image of the wear scar on 0.5Zn–7$Si_3N_4$ coated sample.

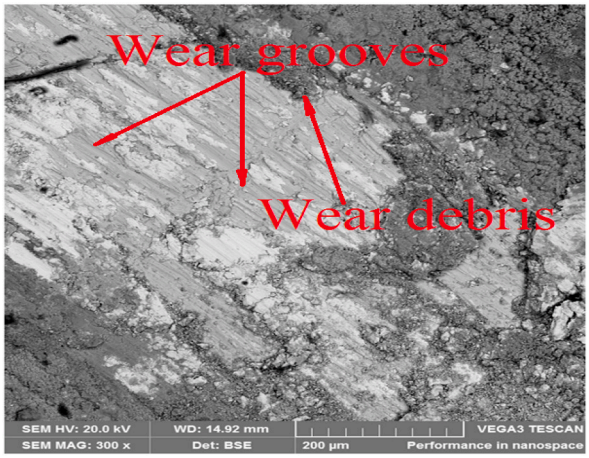


**Fig. 24.** SEM image of the wear scar on 0.3Zn–13$Si_3N_4$ coated sample.

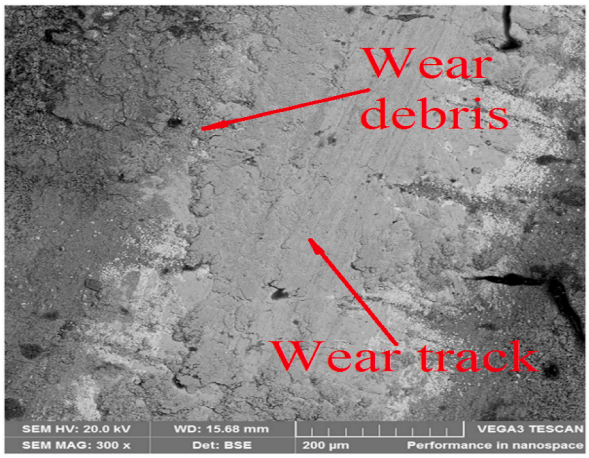


**Fig. 25.** SEM image of the wear scar on 0.5Zn–13$Si_3N_4$ coated sample.

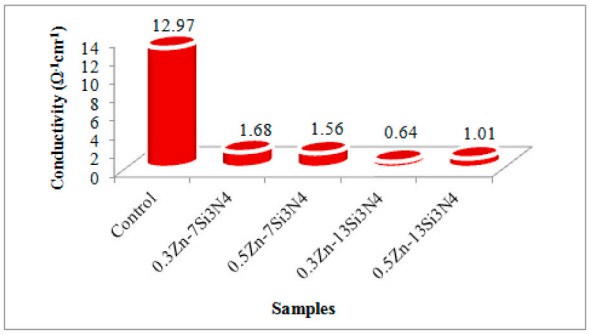


**Fig. 26.** Electrical conductivity of the control sample and coated samples.

Conceptualization. **R.A. Kazeem:** Funding acquisition, Revision of manuscript, Data curation, Conceptualization. **O.O. Oluwole:** Supervision, Validation, Methodology, Investigation, Conceptualization. **T.C. Jen:** Resources, Funding acquisition, Data curation, Supervision. **E.T. Akinlabi:** Investigation, Funding acquisition, Supervision, Data curation, Conceptualization.

## Declaration of competing interest

The authors declare that they have no known competing financial interests or personal relationships that could have appeared to influence the work reported in this paper.

Dear Sir/Ma, This serves to notify you that this manuscript titled "**Production and Characterization of**Low-Density**Zn–$Si_3N_4$ Nanocomposite Coatings for Application in Acidic Media"** is a research work carried out by the authors. There is no competing interest of any kind among the authors or with anyone.

## Acknowledgements

The Mechanical Engineering Department, University of Ibadan is deeply acknowledged for the privilege to carry out this research.

## References

[1] R.B. Heimann, Silicon nitride, a close to ideal ceramic material for medical application, Ceramics 4 (2021) 208–223, https://doi.org/10.3390/ceramics4020016.
[2] P.R. Rao, C.B. Mohan, Study on mechanical performance of silicon nitride reinforced aluminium metal matrix composites Mater, Today Off.: Proceed. 33 (2020) 5534–5538, https://doi.org/10.1016/j.matpr.2020.03.495.
[3] C. Matsunaga, Y. Zhou, D. Kusano, H. Hyuga, K. Hirao, Dielectric breakdown of silicon nitride substrates with various thicknesses, J. Ceramic Soc. Japan 126 (2018) 693–698, https://doi.org/10.2109/jcersj2.18087.
[4] H. Qian, S. Chen, T. Wang, G. Cheng, X. Chen, Z. Xu, D. Yan Silicon nitride modified enamel coatings enable high thermal shock and corrosion resistances for steel protection, Surf. Coat. Technol. 421 (2021), https://doi.org/10.1016/j.surfcoat.2021.127474.
[5] Y. Ling, Y. Tian, X. Wang, J.C. Wang, Enhanced optical and electrical properties of polymer-assisted all-inorganic perovskites for light-emitting diodes Electrical properties of polymer-assisted, Adv. Materall. 28 (2016) 8983–8989, https://doi.org/10.1002/adma.201602513.
[6] D. Dergez, M. Schneider, A. Bittner, N. Pawlak, U. Schmid, Mechanical and electrical properties of RF magnetron sputter deposited amorphous silicon-rich silicon nitride thin films, Thin Solid Films 606 (2016) 7–12, https://doi.org/10.1016/j.tsf.2016.03.029.
[7] L. Khomenkova, P. Normand, F. Gourbilleau, A. Slaoui, C. Bonafos, Optical, structural and electrical characterizations of stacked Hf-based and silicon nitride dielectrics, Thin Solid Films 617 (2016) 143–149, https://doi.org/10.1016/j.tsf.2016.04.036.
[8] L. Xiong, J. Dai, Y. Song, G. Wen, C. Qin Investigation of Photoelectrical Properties with Surface Modifications Using First-Principles Calculations.
[9] Y. Zhao, S. Dong, P. Hu, X. Zhao, C. Hong, Recent progress in synthesis, growth mechanisms, properties, and applications of silicon nitride nanowires, Ceramics Int. 47 (2021) 14944–14965, https://doi.org/10.1016/j.ceramint.2021.02.139.
[10] G. Logesh, M. Rashad, M. Lodhe, U. Sabu, A. Joseph, K.J. Raju, M. Balasubramanian, Mechanical and dielectric properties of carbon fiber reinforced reaction bonded silicon nitride composites, J. Alloys Comp. 767 (2018) 1083–1093, https://doi.org/10.1016/j.jallcom.2018.07.208.
[11] J. Zhang, J. Fan, J. Zhang, J. Zhou, X. Liu, D. Qie, D. Zhang, Developing and preparing interfacial coatings for high tensile strength silicon nitride fiber reinforced silica matrix composites, Ceramics Int. 44 (2018) 5297–5303, https://doi.org/10.1016/j.ceramint.2017.12.143.
[12] Z. Ahmad, S. Khan, S. Hasan, Microstructural characterization and evaluation of mechanical properties of silicon nitride reinforced LM 25 composite, J. Mater. Res. Technol. 9 (2020) 9129–9135, https://doi.org/10.1016/j.jmrt.2020.06.037.
[13] A.C. Reddy, Mechanical properties and fracture behavior of 6061/SiCP metal matrix composites cast by low pressure die casting process, J. Manuf. Technol. Res. 1 (2009) 273–286. ISSN 1943-8095.
[14] R.K. Arya, A. Telang, Silicon nitride as a reinforcement for aluminium metal matrix composites to enhance microstructural, mechanical and tribological behavior, Int. J. Eng. Adv. Technol. 9 (2020) 3366–3374, https://doi.org/10.35940/ijeat.C6032.029320.
[15] O.B. Zgalat-Lozynskyy, O.O. Matviichuk, O.I. Tolochyn, O.V. Ievdokymova, N.O. Zgalat-Lozynska, V.I. Zakiev, Polymer materials reinforced with silicon nitride particles for 3D printing Powd, Metallurg. Met. Ceramics 59 (2021) 515–527, https://doi.org/10.1007/s11106-021-00189-2.
[16] A.K.B. Hanumantharayappa, C. Prasanna, C.C. Ragavendra, C.S. Beekam, L.S. Boluvar, M. Nagaral, S. Rangappa, Synthesis and mechanical characterization of $Si_3N_4$ reinforced copper-tin matrix composites, J. Mech. Behavior Mater. 30 (2021) 199–206, https://doi.org/10.1515/jmbm-2021-0020.
[17] L. Cheng, C. Liu, D. Han, S. Ma, W. Guo, H. Cai, X. Wang Effect of graphene on corrosion resistance of waterborne inorganic zinc-rich coatings, J. Alloys Comp. 774 (2019) 255–264, https://doi.org/10.1016/j.jallcom.2018.09.315.
[18] P.K. Rai, A. Gupta, Investigation of surface characteristics and effect of electrodeposition parameters on nickel-based composite coating Mater, Today Off.: Proceed. 44 (2021) 1079–1085, https://doi.org/10.1016/j.matpr.2020.11.182.
[19] X. Zheng, J. Tan, Q. Zhang, M. Wang, L. Meng, Effect of laser surface texturing depth on the adhesion of electroless plated nickel coating on alumina, Surf. Coat. Technol. 311 (2017) 151–156, https://doi.org/10.1016/j.surfcoat.2017.01.002.
[20] I.G. Akande, O.S.I. Fayomi, O.O. Oluwole, Anticorrosion potential of inhibitive Suphtrim Drug on aluminium alloys in 0.5 M $H_2SO_4$ J, Bio-Tribo-Corros. 6 (2020) 1–8, https://doi.org/10.1007/s40735-020-00429-9.
[21] O.S.I. Fayomi, I.G. Akande, A. P. I. Popoola Corrosion protection effect of chitosan on the performance characteristics of A6063 alloy J, Bio-Tribo-Corros. 4 (2018) 1–6, https://doi.org/10.1007/s40735-018-0192-6.
[22] M.A. Deyab, Electrochemical investigations on pitting corrosion inhibition of mild steel by provitamin B5 in circulating cooling water, Electrochim. Acta 202 (2016) 262–268, https://doi.org/10.1016/j.electacta.2015.11.075.
[23] R. Qin, Y. Du, Z. Xu, M. Lu, Anodic polarization behavior of X80 steel in $Na_2SO_4$ solution under high potential and current density Conditions, Materials 12 (2019) 1–14, https://doi.org/10.3390/ma12030394.
[24] L. Li, M. Mahmoodian, C.Q. Li, D. Robert, Effect of corrosion and hydrogen embrittlement on microstructure and mechanical properties of mild steel Const, Build. Mater. 170 (2018) 78–90, https://doi.org/10.1016/j.conbuildmat.2018.03.023.
[25] C.M. Praveenkumar, T.V. Venkatesha, K. Vathsala, K.O. Nayana, Electrodeposition and corrosion behavior of Zn–Ni and Zn–Ni–$Fe_2O_3$ coatings, J. Coat. Technol. Res. 9 (2012) 71–77, https://doi.org/10.1007/s11998-011-9322-5.
[26] J. Sheng, X. Shen, Y. Wang, Q. Xu, X. Zhang, Microstructure and corrosion behavior of electrodeposited Zn-TiN composite coatings, Mater. Corros. 70 (2019) 1044–1055, https://doi.org/10.1002/maco.201810576.
[27] C.C. Enyi, V.S. Aigbodion, E.T. Akinlabi, C.A. Mgbemene, Electrochemical and mechanical study of co-deposited Zn–ZnO-snail shell particles composites coating on mild steel, Int. J. Adv. Manuf. Technol. 96 (2018) 4313–4319, https://doi.org/10.1007/s00170-018-1757-8.
[28] C.P. Kumar, T.V. Venkatesha, Electrodeposition, characterization and corrosion behavior of Ni–$Si_3N_4$ composites Phys, Scrip. 86 (2012) 015804, 1402-4896/86/1/015804.
[29] H. Liang, Y. Zeng, K. Zuo, Y. Xia, D. Yao, J. Yin Mechanical properties and thermal conductivity of $Si_3N_4$ ceramics with YF3 and MgO as sintering additives, Ceramics Int 42 (2016) 15679–15686, https://doi.org/10.1016/j.ceramint.2016.07.024.